ADVANCED MATERIALS
www.advmat.de

Ultrahigh Conductive MXene Films for Broadband Electromagnetic Interference Shielding

Ju-Hyoung Han, Jaeeun Park, Mincheal Kim, Sungwoo Lee, Jin Myeong Heo, Young Ho Jin, Yujin Chae, Juwon Han, Jaewon Wang, Shi-Hyun Seok, Yeoseon Sim, Gangil Byun, Gun-Do Lee, EunMi Choi,* and Soon-Yong Kwon**

Broadband and ultrathin electromagnetic interference (EMI)-shielding materials are crucial for efficient high-frequency data transmission in emerging technologies. MXenes are renowned for their outstanding electrical conductivity and EMI-shielding capability. While substituting nitrogen (N) for carbon (C) atoms in the conventional MXene structure is theoretically expected to enhance these properties, synthesis challenges have hindered progress. Here, it is demonstrated that $Ti_xC_yN_{x-y-1}T_z$ MXene films with optimized N content achieve a record-high electrical conductivity of 35 000 S cm^{-1} and exceptional broadband EMI shielding across the X (8–12.4 GHz), K_a (26.5–40 GHz), and W (75–110 GHz) bands—outperforming all previously reported materials even at reduced thicknesses. By synthesizing a full series of high-stoichiometric $Ti_xAlC_yN_{x-y-1}$ MAX phases without intermediate phases, the impact of N substitution on the physical and electrical properties of $Ti_xC_yN_{x-y-1}T_z$ MXene flakes is systematically explored, achieving complete composition tunability in both dispersion and film forms. These findings position $Ti_xC_yN_{x-y-1}T_z$ MXenes as promising candidates for applications spanning from conventional lower-frequency domains to next-generation sub-THz electronics.

1. Introduction

Driven by the rapidly growing demand from high-frequency bands due to the rise of wireless communication, autonomous vehicles, and system-in-package, the need for efficient data transmission at high frequencies has significantly increased.[1] Traditional lower-frequency bands, including the X-band (8–12.4 GHz), are now saturated, prompting a shift toward developing technologies that operate in sub-terahertz (sub-THz) high-frequency bands, such as the K_a (26.5–40 GHz), V (40–75 GHz), and W (75–110 GHz) bands. These higher frequency ranges pose severe electromagnetic interference (EMI) challenges that can result in data loss, system malfunctions, and potential health risks,[2,3] necessitating novel materials with superior EMI-shielding capabilities at reduced thicknesses. Current EMI-shielding materials, such as metals and ferrites, are effective only up to ≈20 GHz (ref. [4]). Despite progress in developing high-frequency EMI-shielding materials that operate at frequencies up to 90 GHz or higher, their performance remains suboptimal.[5] Furthermore, these materials tend to be bulky and rigid, limiting their practical applications in modern electronics.

2D transition metal carbides and nitrides (MXenes) exhibit exceptional EMI-shielding capabilities in the X-band, outperforming other materials at comparable low thicknesses. In addition to their high performance, MXenes offer advantages such as low density and lightweight characteristics compared to metals.[6,7] Since their discovery in 2011, the

J.-H. Han, J. Park, Y. H. Jin, Y. Chae, J. Han, J. Wang, S.-H. Seok, Y. Sim, S.-Y. Kwon
Department of Materials Science and Engineering and Graduate School of Semiconductor Materials and Devices Engineering
Ulsan National Institute of Science and Technology (UNIST)
Ulsan 44919, Republic of Korea
E-mail: sykwon@unist.ac.kr

The ORCID identification number(s) for the author(s) of this article can be found under https://doi.org/10.1002/adma.202502443

DOI: 10.1002/adma.202502443

M. Kim, J. M. Heo, G. Byun, E. Choi
Department of Electrical Engineering
Ulsan National Institute of Science and Technology (UNIST)
Ulsan 44919, Republic of Korea
E-mail: emchoi@unist.ac.kr

S. Lee, G.-D. Lee
Department of Materials Science and Engineering
Seoul National University
Seoul 08826, Republic of Korea
E-mail: gdlee@snu.ac.kr

electrical conductivity of MXenes has rapidly developed from 3000 to 20 000 S cm^{-1} (refs. [6–10]), reflecting advances in synthetic techniques and material quality. However, their performance in sub-THz frequency regimes remains underexplored, and achieving a high EMI shielding effectiveness (SE) in the X-band still often requires relatively thick films on the order of tens of micrometers. Given the direct correlation between electrical conductivity and EMI SE in MXenes,[6–8] further enhancement of their intrinsic electrical properties is essential. Recent studies show that structurally and chemically engineered MXenes can meet the stringent demands of modern electronics by enabling optimal EMI shielding through the synergistic integration of electrical conductivity, absorption, mechanical strength, and stability.[11,12]

Crucially, the physical and electrical properties of MXenes are inherently linked to their precursor MAX phases, where M, A, and X denote transition metals, typically Al, and C or N, respectively.[13–16] Previous studies attempted to incorporate N atoms in $Ti_3C_2T_z$ by synthesizing MAX phases or through ex situ doping because theoretical calculations suggest that N substitution enhances the physical and electrical properties of MXenes.[17–19] However, the synthetic N-substituted MXenes exhibit lower conductivities than $Ti_3C_2T_z$, likely because of the difficulty in A-layer etching and the presence of intermediate species that affect the precursor MAX phase quality.[7,20–22] Achieving a high-quality X-site solid solution (XSS) MAX phase is particularly challenging owing to the low stability of the nitride MAX phase and the complexity of intermediate species in the M-A-C-N quaternary system.[17,23–25] Thus, preparing a high-stoichiometric XSS MAX phase is essential to produce high-quality XSS MXenes, and the effect of N substitution on XSS MXene flakes and their films is needed to be elucidated for their potential applications.

In this study, we report a substantial enhancement in the electrical conductivity of MXene films of up to 35000 S cm^{-1} through N substitution at the X-site in XSS MAX phases. This enhancement was attributed to the successful synthesis of high-stoichiometric XSS MAX phases without the formation of intermediate phases and the elucidation of the effects of N substitution on the physical properties of these phases. With precisely controlled A-layer etching coupled with a modified synthesis approach over N content, we synthesized the full series of XSS MXene flakes for $Ti_3C_{2-x}N_x$ (x = 0–0.9) and $Ti_4C_{3-y}N_y$ (y = 1.8–3) in both dispersion and film forms. Consistent with the transfer-matrix simulations, the XSS MXene films with optimized N content exhibited remarkable EMI SE exceeding 100 dB at reduced thicknesses of only 6–15 µm across a wide range of frequencies, including X, K_a, and W bands, surpassing previously reported materials in terms of EMI-shielding capability.

2. Results and Discussion

2.1. Role of Nitrogen in XSS MAX Phases

High-stoichiometric XSS MAX phases, specifically $Ti_3AlC_{2-x}N_x$ (x = 0–0.9) and $Ti_4AlC_{3-y}N_y$ (y = 1.8–3), were synthesized via a closed-crucible system that regulated N loss during sintering (**Figure 1a**; Figures S1–S5, Table S1, Note S1, Supporting Information for more details). The X-ray diffraction (XRD) patterns of the full series of XSS MAX phases reveal well-defined crystal planes, confirming the absence of intermediate MAX phases, and validating our high-quality synthesis protocol (Figure 1b; Figures S4 and S5, Supporting Information). A distinct miscibility range, defined by an $N/(N + C)$ ratio of 0.5 to 0.55, was identified, signifying a phase transformation from M_3AX_2 (312-MAX) to M_4AX_3 (413-MAX) with increasing N content, thereby underscoring the challenge of achieving a C/N stoichiometry of 1 in MAX phases such as $Ti_3AlC_1N_1$ and $Ti_4AlC_{1.5}N_{1.5}$.

To understand the experimental results for the synthesis of XSS MAX phases as a function of the N content, we performed density functional theory (DFT) calculations for the formation energies of the 312- and 413-MAX phases (Note S2, Supporting Information). Several possible combinations of compounds are involved in the synthesis reaction of the XSS MAX phases that satisfy the stoichiometry of the final MAX phase. As shown in Figure 1c and Figure S6 (Supporting Information), the calculation results for the DFT formation energy describe the experimental results well, where the 312-MAX phase was synthesized when C was more abundant than N, and the 413-MAX phase was synthesized when N was more abundant than C. This also explains the reversal of the synthesis of the 312- and 413-MAX phases when C and N are present in equal amounts.

The peak shifts in the enlarged XRD patterns were aligned with N substitution, reducing the unit cell volume owing to the smaller size of N (Figure S7, Supporting Information). Specifically, as x increased from 0 to 0.9, the a- and c-lattice parameters of 312-MAX decreased from 3.084 to 3.048 Å and from 18.646 to 18.395 Å, respectively, while as y decreased from 3 to 1.8, the a- and c-lattice parameters of 413-MAX increased from 2.989 to 3.013 Å and from 23.397 to 23.444 Å, respectively (Figure 1d,e). Particularly, the deviation between the experimental and calculated values enlarged especially along c-axis, suggesting a greater contraction in the unit cell volume than predicted, presumably because of increasing vacancy formation derived from mixed element lattice disorder.[24,26]

Scanning electron microscopy (SEM) images show the typical layered structure of the MAX phases with no identifiable differences between the 312- and 413-MAX phases (Figure 1f), and energy-dispersive X-ray spectroscopy (EDS) mapping confirmed a uniform distribution of each element (Figure S8, Supporting Information). The intensities associated with C and N strictly followed the trends observed for x and y for 312- and 413-MAX phases, respectively (Figure 1g). X-ray photoelectron spectroscopy (XPS) confirmed the successful substitution of the X element (Figure 1h; Figure S9, Supporting Information). The observed shifts in the binding energies of Ti $2p_{3/2}$, ranging from 454.8 to 455.2 eV with increasing N contents, are indicative of the formation of Ti-C and Ti-N bonds, within the MAX phases, reflecting the success of the substitution process. Likewise, shifts in the binding energies of N 1s, from 397.2 to 397.4 eV, and C 1s, from 281.8 to 282.1 eV, further signify the presence of mixed Ti-C and Ti-N bonds within the MAX phases, confirming the success of the substitution process.

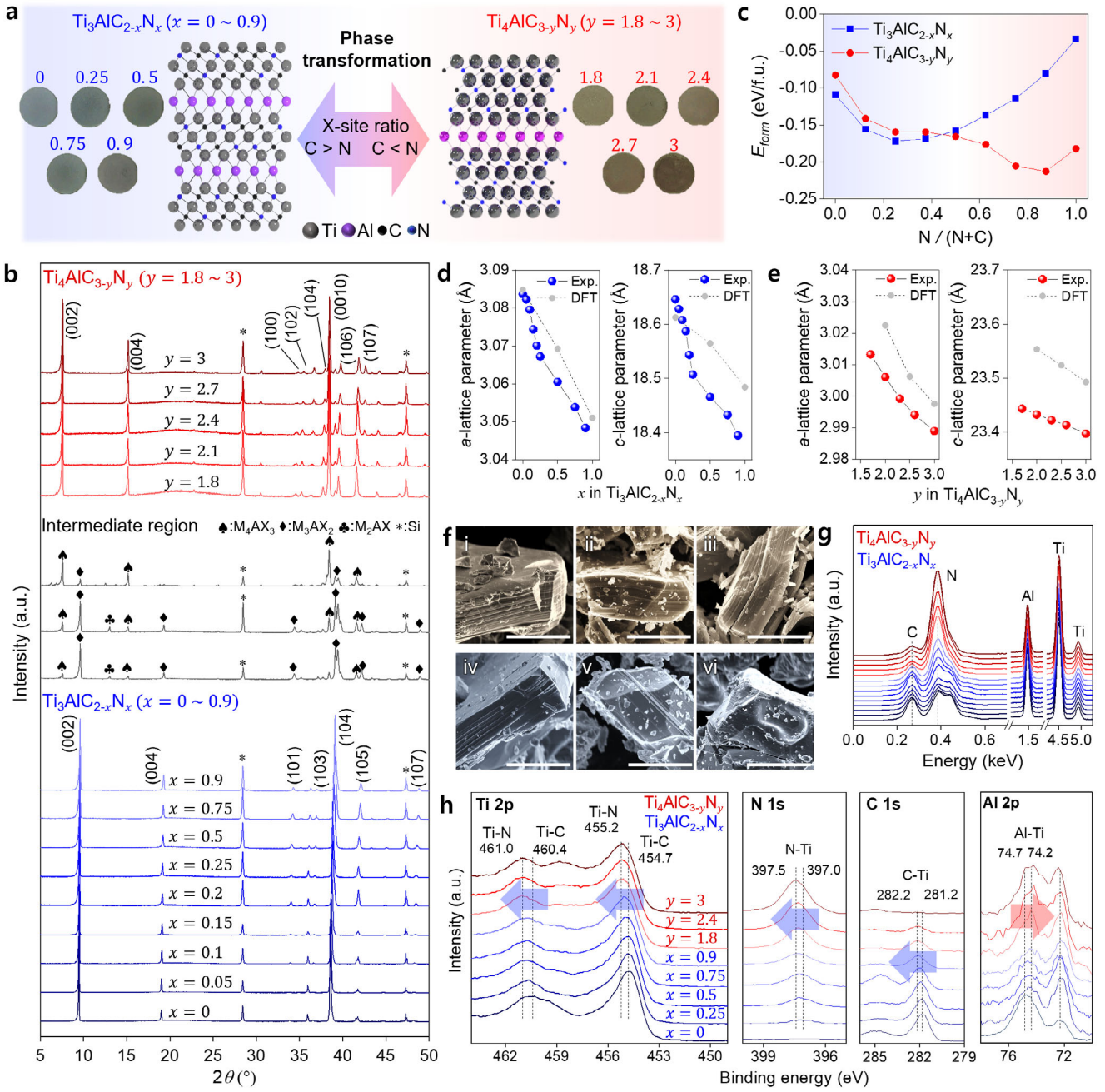

Figure 1. Synthesis and characterizations of XSS MAX phases. a) Schematic illustration and photographs of cold-pressed pellets of XSS MAX phases. b) XRD patterns of 312- (blue) and 413- (red) MAX phases, and intermediate range (black). Si is used for peak shift calibration. c) Calculated formation energy of 312- (blue) and 413- (red) MAX phases. d, e) Experimental and calculated *a*-lattice (left) and *c*-lattice (right) parameters of (d) 312- and (e) 413-MAX phases. f) Representative SEM images of (i–iii) 413-MAX ($Ti_4AlC_{3-y}N_y$: $y = 1.8$, 2.4, and 3.0) and (iv–vi) 312-MAX ($Ti_3AlC_{2-x}N_x$: $x = 0$, 0.5, and 0.9). Scale bars indicate 10 μm. g) EDS spectra of full-series 312- (blue) and 413- (red) MAX phases. h) XPS spectra of Ti *2p*, N *1s*, C *1s*, and Al *2p* of 312- (blue) and 413- (red) MAX phases.

2.2. Effect of N Substitution on the Physical Properties of XSS MAX Phases

To elucidate the lattice disorder induced by N substitution at X-sites, the Raman spectra of the full series of the XSS MAX phases were analyzed (**Figure** 2a,b). The substitution of X elements led to notable shifts in vibrational peaks within the high energy region of 500 to 700 cm^{-1}, corresponding to the X-element-dominant vibrational states.[27,28] Specifically, the ω_6 peak, associated with the out-of-plane vibrational mode red-shifted from 657.3 to 648.7 cm^{-1}, while the in-plane vibrational modes, ω_{5a} and ω_{5b} peaks, blue-shifted from 625.6 to 638.7 cm^{-1} as the x value increased in 312-MAX. Moreover, the sharpening of the ω_2 and ω_3 peaks as x increased from 0 to 0.25 indicates enhanced

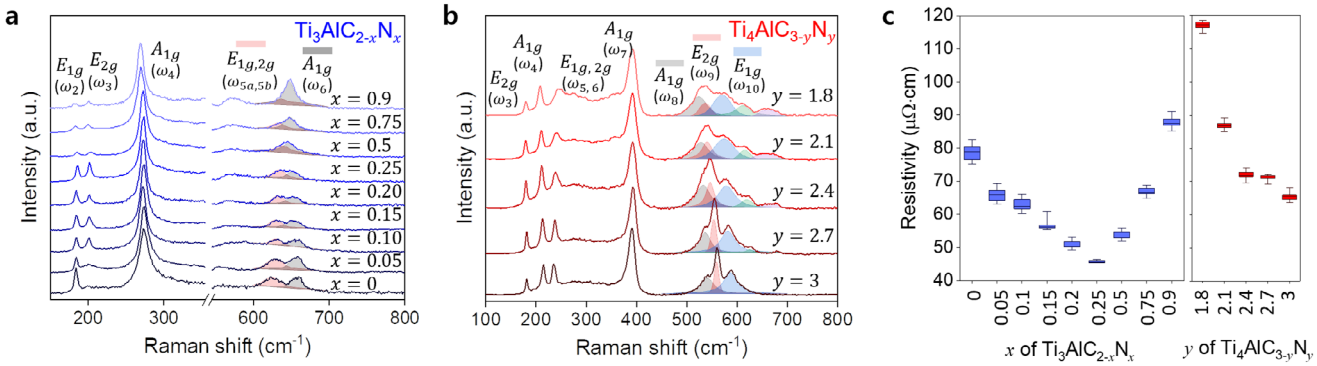

Figure 2. Physical properties of XSS MAX phases. a, b) Raman spectra of (a) 312- and (b) 413-MAX phases. c) Electrical resistivities of (left) 312- and (right) 413-MAX phases.

lattice order, while their subsequent broadening and disappearance beyond $x = 0.5$ signify the onset of lattice disorder. For 413-MAX, the $\omega_{8\text{-}10}$ peaks exhibited significant red shifts and broadening, with new bands emerging at 620 and 660 cm^{-1} as y decreased from 3 to 1.8, indicative of lattice symmetry disruption as the mixed C/N fraction increases.[22,29] The in-plane vibrational peaks of ω_5 and ω_6 associated with Ti-Al vibrations blue-shifted and broadened from 235.4 to 245.7 cm^{-1} as y decreased from 3 to 1.8. Overall, N substitution induces severe internal strain in both the M-X and M-A layers within the XSS MAX phases (Figure S10, Supporting Information).

The electrical resistivity of the XSS MAX phases was measured to further assess the extent of lattice disorder (Figure 2c; Table S2, Supporting Information). In 312-MAX, the resistivity decreased from 78.54 ± 2.14 to 45.70 ± 0.37 μΩ cm up to $x = 0.25$, which indicates that N substitution enhanced electrical conductivity, presumably by improving the lattice structure and reducing the electron scattering. However, as x further increased to 0.9, a subsequent increase in resistivity to 87.61 ± 1.58 μΩ cm indicates that excessive N substitution results in lattice disorder, which impedes electron transport. In 413-MAX, a similar trend was observed, where the electrical resistivity consistently decreased from 117.01 ± 1.31 to 65.52 ± 1.37 μΩ cm as y increased from 1.8 to 3, which indicates a strong correlation between the N content and the enhanced electrical properties, possibly because of improved lattice uniformity at higher N levels. These results suggest that the solid-solution content plays a crucial role in modulating the electrical properties of the XSS MAX phases by influencing both the lattice order and defect states.

2.3. A-Layer Etching Kinetics of XSS MAX Phases

Theoretical predictions on the feasibility of exfoliation emphasized the differences in bonding strengths between the M-A and M-X layers.[15,30] N substitution results in shorter Ti—N bonds and an increased number of valence band electrons in the Ti—Al bonds, reducing the bond strength difference between Ti—Al and Ti—N. This alteration in bonding strength complicates the selective etching of layer A, thereby intensifying the challenges associated with the production of nitride MXenes.[31] To investigate this effect, the A-layer etching kinetics of the XSS MAX phases were systematically studied using a combination of HF and HCl (Figure S11, Supporting Information). The XRD patterns confirmed that the complete conversion of 312-MAX to $Ti_3C_{2-x}N_xT_z$ (32-MXene) required 36 h at $x = 0$, and the conversion time extended to 48 h as x increased to 0.1. Interestingly, as the N content further increased to $x = 0.9$, the etching time gradually decreased from 36 to 18 h. For 413-MAX, the XRD patterns showed an absence of $Ti_4C_{3-y}N_yT_z$ (43-MXene) peaks at $y = 2.7$ and 3.0, indicating that increased N concentrations hinder 43-MXene formation (Figure S12, Supporting Information). In contrast, at lower N contents, the conversion to 43-MXene occurred with an etching time of at least 60 h. The SEM images of the etched XSS MAX phases revealed that a higher N content correlated with increased void formation within the crystal structure (Figure S13, Supporting Information).

To quantitatively assess the impact of nitrogen substitution on defect formation, we defined the etch pit formation rate (EPFR) and etch pit density (EPD) and measured them for 32-MXene samples with $x = 0$, 0.1, 0.25, 0.5, and 0.9 (Figure S14, Supporting Information). EPFR represents the ratio of pit-containing particles to the total number of particles, whereas EPD is defined as the number of etch pits per unit area within the multilayer MXene. We found that samples with $x \leq 0.1$ exhibited minimal defect formation (EPFR ≈10–13%, EPD ≈3.5–3.8 × 10^5 cm^{-2}), whereas both EPFR and EPD increased sharply from $x = 0.25$ onward, reaching up to ≈73% and ≈2.1 × 10^6 cm^{-2}, respectively, at $x = 0.9$). These observations suggest that N substitution enhances the bond strength, thereby reducing the probability of H^+ or F^- ion assault on the A-layer, complicating selective A-layer etching, and facilitating void formation through the M-X layer. Consequently, the M-X layer dissolved immediately upon A-layer etching, preventing the preservation of the MXene structure at elevated N concentrations, specifically at $y = 2.7$ and 3.0 (Figure S15, Supporting Information). Moreover, the accelerated conversion at $x = 0.9$ and $y = 1.8$ indicates that these voids enhance A-layer etching by providing etchants with an increased surface area for interaction (Figure S16, Supporting Information).

To synthesize delaminated 43-MXenes, we modified this method using LiF, HBr, and LiBr (Figure S17a, Supporting Information). The synthesis of void-free nitride MXenes was facilitated by protecting the exfoliated MXene from the etchant through the addition of a sufficient amount of Li cations[32] (Figure S17b,

Supporting Information). The XRD pattern displays clear peaks at 2θ ≈4.9°, corresponding to the (002) peak of 43-MXene in the all *y* fraction, indicating that the modified synthesis method can effectively produce MXene via a solution (Figure S18, Supporting Information). XPS analysis confirmed the absence of Al and revealed -O, -F, and -Br terminations on the 43-MXene surface[33] (Figures S19 and S20, Supporting Information). However, the modified etching process for the synthesis of defect-free 43-MXene needs to be developed considering the presence of a green supernatant (i.e., dissolved titanium fluoride ions), which was generated during the etching process[34] (Figure S21, Supporting Information). The yields of delaminated XSS MXenes across the entire composition range—including 32-MXene synthesized via an acid-based method and 43-MXene via a saturated salt solution—are provided in Note S3 (Supporting Information) (Figure S22, Supporting Information).

2.4. Effect of N Substitution on the Electrical Properties of XSS MXenes

Figure 3a presents representative photographs of the synthesized i) multi-layered XSS MXene (m-MXene) and ii) delaminated XSS MXene (d-MXene) in both dispersion and film forms. The representative atomic force microscopy (AFM) images show the successful delamination of MXene into a single layer with an average thickness of ≈1.8 nm for 32-MXene and ≈2.7 nm for 43-MXene (Figure S23, Supporting Information). The characteristic colors of the XSS m-MXene and d-MXene films transition from purple to brown as the N content increases. Notably, the color of the d-32-MXene dispersions changes from green to blue-green as *x* increases from 0 to 0.5, eventually turning gray-green at $x = 0.9$. Similarly, the color of d-43-MXene transitions from gray-green to dark blue-green as *y* increases from 1.8 to 3. The ultraviolet-visible-near infrared (UV-vis-NIR) absorption spectra revealed the origin of these color changes (Figure 3b). As the N content increases, the absorption peaks gradually blue-shifted from 780 to 640 nm and from 320 to 260 nm for 32-MXene. Further blue shifts in the UV region, along with a broad and intense absorption band in the NIR region, were observed for 43-MXene. Notably, the extent of NIR absorption increases with increasing N content. These results suggest that N substitution significantly affects the electronic state and structural differences in MXenes.

The density of states (DOS) was calculated to further investigate the electronic structures of the XSS MXenes (Figure 3c; Figure S24, Table S3, and Note S4, Supporting Information for more details). The overall states of $Ti_3C_{2-x}N_xO_2$ shift downward as *x* increases, similar to the behavior of 312-MAX (ref. [25]), owing to the emergence of deep states originating from the Ti *3d*-N *2p* hybridized state (Figure S25, Supporting Information). As these states shift downward, the DOS at the Fermi level increases, indicating that N substitution enhances the electrical properties of the material. A similar trend is observed in $Ti_4C_{3-y}N_yO_2$ as well (see Figures S26 and S27, Supporting Information for details). Considering these electronic states, the shift observed in the absorption peaks of the XSS MXene is presumably owing to its intrinsic electronic structure, which is influenced by inter- and intra-band transitions.[35–38]

To characterize the effect of N substitution on electrical conductivity, free-standing XSS MXene films were fabricated via vacuum filtration. Cross-sectional SEM image and EDS mapping show well aligned structure of the XSS MXene films and uniform distribution of each element (Figure 3d; Figure S28, Supporting Information). Thermal annealing of the XSS MXene films was carried out at 250 °C for 2 h under vacuum conditions to promote the de-intercalation of H_2O molecules from the interlayers and the desorption of surface-bound -OH groups.[7] SEM-EDS analysis confirmed that, although the oxygen content decreased, the C and N ratios remained nearly unchanged after the annealing process (Table S4, Supporting Information). The XRD patterns of the annealed XSS MXene films show characteristic basal-plane (002)-dominant alignments (Figure 3e). As shown in the XRD patterns of the 32-MXene films, the (002) peak gradually shifted toward lower 2θ values and became broader with increasing nitrogen content, indicating an expansion of interlayer spacing and a reduction in film alignment (Figure S29, Supporting Information). At low nitrogen contents ($x = 0$–0.1), both the interlayer spacing and the full width at half maximum (FWHM) remained nearly constant, suggesting minimal structural changes. Notably, the interlayer spacing of $Ti_3C_2T_z$ decreased to 2θ ≈8.9° at an annealing temperature of 250 °C, while $Ti_4N_3T_z$ required annealing at 500 °C to reach 2θ ≈6.6° (Figure S30, Supporting Information). We note that free-standing XSS MXene films (≈5 µm) exhibited exceptional mechanical flexibility and durability—maintaining stable electrical resistance under severe bending (radius ≈1.1 mm) (Table S5 and Figure S31, Supporting Information).

Remarkably, the electrical conductivity of the annealed $Ti_3C_{2-x}N_xT_z$ increased from 22394 ± 1212 (at $x = 0$) to 34520 ± 1785 (at $x = 0.1$) S cm^{-1} (Figure 3f; Table S6, Supporting Information). However, as the N substitution increased to $x = 0.9$, the electrical conductivity gradually decreased to 7590 ± 375 S cm^{-1}. Notably, the electrical conductivity of 32-MXene remained equal to or higher than its initial value up to $x = 0.2$ (i.e., 27440 ± 1366, 28732 ± 1048, and 23454 ± 1214 S cm^{-1} at $x = 0.05$, 0.15, and 0.2, respectively). To elucidate the origin of this composition-dependent behavior, Hall effect measurements were performed (Figure S32 and Table S7, Supporting Information). As the nitrogen content increased from $x = 0$ to 0.1, the carrier concentration significantly increased, reaching ≈4.72×10^{22} cm^{-3}. This increase in charge carrier density played a dominant role in enhancing electrical conductivity, despite a concurrent decrease in carrier mobility from ≈8.06 to ≈3.92 cm^2 V^{-1} s^{-1}. The mobility reduction is attributed to impurity scattering caused by substitutional nitrogen atoms replacing carbon. Beyond $x = 0.1$, both carrier concentration and mobility exhibit a decreasing trend. This suggests that N substitution enhances the electrical conductivity of MXene up to a certain point, similar to its effects on the MAX phases. However, further increases in N content lead to defect formation during etching, including the development of voids and surface Ti vacancies,[39] which in turn results in reduced electrical conductivity.

To evaluate the impact of structural defects on the electronic states, we performed DOS calculations for XSS MXenes with varying concentrations of surface Ti vacancies. The results indicate that the introduction of Ti vacancies significantly reduces the DOS near the Fermi level (Figure S33, Supporting Information). In addition, structural defects disrupt charge transport pathways

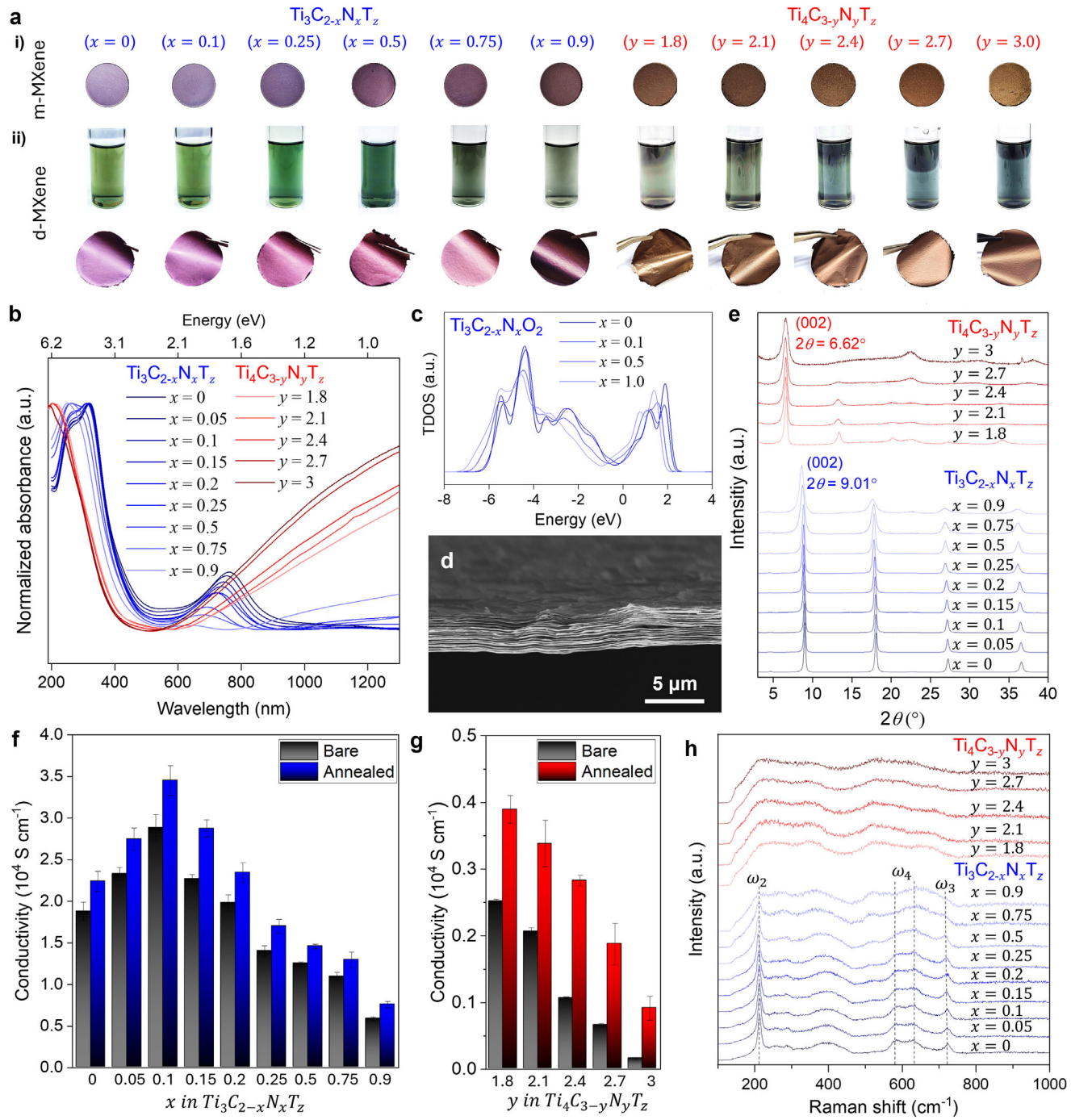

Figure 3. Effect of N substitution on the physical and electrical properties of XSS MXenes. a) Photograph of synthesized XSS MXenes showing: i) cold-pressed multi-layered MXene (m-MXene), ii) delaminated MXene (d-MXene) solution (top) with a vacuum-filtrated free-standing film (bottom). b) UV–vis–NIR absorption spectra of 32- (blue) and 43- (red) MXenes. c) Total DOS of $Ti_3C_{2-x}N_xO_2$. d) Cross-sectional SEM image of the $Ti_3C_{1.9}N_{0.1}T_z$ film. e) XRD patterns of annealed 32- (blue) and 43- (red) MXene films. f, g) Electrical conductivities of (f) 32- and (g) 43-MXenes before and after annealing. h) Raman spectra of 32- (blue) and 43- (red) MXene films.

in the MXene films. Specifically, the presence of voids and lattice imperfections impairs both inter- and intra-flake electrical conduction. The inter-flake resistance increases due to flake misalignment caused by structural voids, whereas the intra-flake conductivity decreases as a result of defect-induced lattice disorder and enhanced electron scattering, as previously reported.[21,40,41] These theoretical and experimental findings support our interpretation that the observed decline in conductivity beyond $x = 0.1$ is due to the progressive accumulation of etching-induced defects, such as voids and surface Ti vacancies, which

increasingly disrupt the electronic structure and suppress charge transport.

Consequently, the electrical conductivity of 43-MXene steadily decreased from 3895 ± 209 to 915 ± 178 S cm^{-1} as y increased from 1.8 to 3 (Figure 3g). The Raman spectra of the 43-MXene films exhibited broader vibrational bands than those of the MAX phase (Figure 3h), probably owing to the presence of defects introduced during the acid etching process. Nevertheless, the ω_2, ω_3, and ω_4 peaks were observable at $x = 0$ to 0.25 in 32-MXene films, which suggests the retention of high electrical conductivity within this composition range.[42] In particular, the ω_2 peak shifted toward lower wavenumbers with increasing nitrogen content, from 213 cm^{-1} in $Ti_3C_2T_z$ to ≈210 cm^{-1} in $Ti_3C_{1.25}N_{0.75}T_z$, suggesting that nitrogen substitution induces local structural softening (Figure S34, Supporting Information).

2.5. Broadband EMI-Shielding Performance of XSS MXene Films

Figure 4a demonstrates the EMI SE of $Ti_3C_{1.9}N_{0.1}T_z$ films across the X-, K_a-, and W-bands at varying thicknesses. The dashed line at ≈116 dB indicates the limit of detection (LD) for the measurement system (Figure S35, Supporting Information). Notably, the EMI SE increases significantly at higher frequencies, achieving the LD with a film thickness of only 6 µm in the W-band. In comparison, films with lower conductivity values require larger thicknesses to achieve the same SE, which emphasizes the critical role of electrical conductivity in high-frequency EMI shielding (Figure S36, Supporting Information). The 43-MXene films with lower conductivity values exhibited reduced EMI SEs in the X-band (Figure S37, Supporting Information).

Compared to Cu and Al foils, the $Ti_3C_{1.9}N_{0.1}T_z$ film exhibits a superior EMI SE (Figure 4b; Figure S38, Supporting Information). The reflection SE (SE_R) is similar to that of bulk metals, while its absorption SE (SE_A) is markedly higher, resulting in an enhanced total SE (SE_T). To understand the mechanisms responsible for this superior performance, a transfer-matrix model was employed to analyze the interaction of electromagnetic waves (EMWs) with MXene films (Figure S39 and Note S5, Supporting Information).

Figure 4c presents the transmittance and reflectance of the MXene film at 10 GHz as functions of electrical conductivity (100–35 000 S cm^{-1}) and thickness (0–10 µm). The reflectance increases at higher conductivity values and saturates at values above 0.998, which implies that more than 99.8% of the incident EMWs are reflected. Concurrently, the transmittance steadily decreases to nearly zero with the increase in electrical conductivity, effectively blocking EMWs. This indicates that SE_R saturates at ≈25 dB and that SE_A continues to increase at higher conductivity values, resulting in a substantial overall increase in SE_T (Figure S40, Supporting Information). This exceptional EMI-shielding performance of the MXene films compared to bulk metals arises from fundamental differences in their mechanisms.

To clarify the EMI shielding mechanisms of XSS MXene, we investigated the dominant loss pathways—ohmic loss, interface scattering, and polarization loss—through theoretical analysis and targeted experiments (Note S6, Supporting Information). Although its metallic conductivity ($\sigma \approx 3.5 \times 10^4$ S cm^{-1}) suggests a dominant contribution from ohmic loss, XSS MXene exhibited higher SE_A and SE_T values than Cu and Al, despite its lower conductivity. This indicates the presence of additional attenuation mechanisms. Ultrathin film experiments (≈δ/10, where δ is the skin depth) revealed that XSS MXene effectively suppresses multiple internal reflections, a phenomenon attributed to strong internal scattering facilitated by its multilayered architecture (Figures S41 and S42, Supporting Information). Dielectric loss contributions, evaluated using a complex permittivity-based model, were found negligible under high-conductivity conditions, with attenuation constants orders of magnitude lower than those from conductive models, even at high dielectric loss tangent (tan δ) (Figure S43, Supporting Information). As XSS MXene is non-magnetic ($\mu_r = 1$), magnetic losses were excluded. These results support the dominant roles of ohmic loss and interface scattering, and future work will include direct permittivity and permeability measurements to refine the shielding model.

Figure 4d presents the calculated EMI SE_T of the MXene film in a frequency range of 0.1–100 GHz. The difference in SE_T between films having electrical conductivities of 15 000 and 35 000 S cm^{-1} is ≈10 dB at lower frequencies such as 0.1 GHz. However, this difference becomes more pronounced at higher frequencies such as 100 GHz. For films with an electrical conductivity of 15 000 S cm^{-1}, a ≈10-µm-thick film is required to achieve an EMI SE_T of 100 dB. In contrast, a film with an electrical conductivity of 35 000 S cm^{-1} achieves the same SE_T at a thickness of only 5 µm. This enhanced performance at higher frequencies is attributed to the rapid reduction in transmittance within this range, decreasing to 10^{-10}, corresponding to EMI SE_T exceeding 100 dB (Figure S44, Supporting Information). These results align well with experimental observations, emphasizing the importance of the optimization of both conductivity and film thickness to maximize the SE in advanced high-frequency applications.

To validate the exceptional EMI-shielding performance of $Ti_3C_{1.9}N_{0.1}T_z$, the films were benchmarked against other MXenes, metal foils, and carbon-based materials reported over the past five years (Figure 4e; Table S8, Supporting Information). $Ti_3C_{1.9}N_{0.1}T_z$ achieves higher EMI SE values at lower thicknesses compared to other materials, with an excellent agreement between experimental data and transfer-matrix calculations. Notably, the annealed $Ti_3C_{1.9}N_{0.1}T_z$ films demonstrated outstanding ambient stability over 230 days, showing only minor degradation in EMI SE (≈4 dB) for thinner samples (1.2 µm), attributable to slight surface oxidation (Figure S45, Supporting Information). Under harsh humid conditions, the annealed $Ti_3C_{1.9}N_{0.1}T_z$ films further demonstrated superior environmental stability—exhibiting minimal EMI SE loss and nearly full recovery after vacuum annealing—unlike Cu and Al foils, which suffered irreversible degradation due to corrosion (Figure S46, Supporting Information). In addition, spray-coated $Ti_3C_{1.9}N_{0.1}T_z$ films exhibited tunable transparency on glass and PET substrates (Figure S47, Supporting Information), demonstrating the scalability and flexibility of XSS MXene for optically transparent and EMI-shielding applications. These results underscore the strong potential of XSS MXene films for real-world applicability. Furthermore, the specific SE per unit thickness (SSE t^{-1}) highlights the superior performance of XSS MXenes for advanced EMI-shielding applications (Figure S48, Supporting Information). Benchmark comparisons in the W-band additionally reaffirm the high quality and reliability of these films for

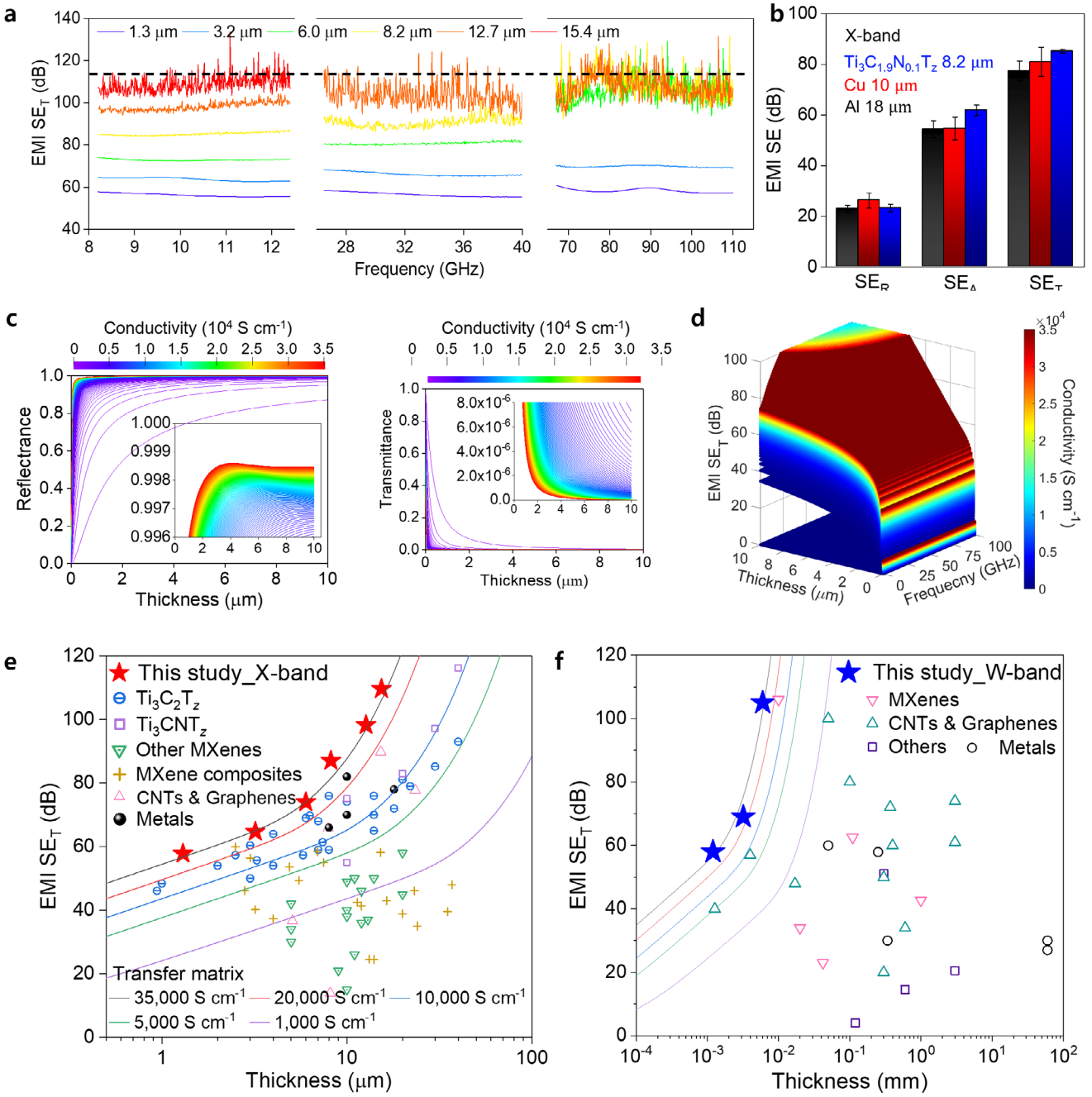

Figure 4. Broadband EMI-shielding characteristics of XSS MXene films. a) EMI SE$_T$ values of $Ti_3C_{1.9}N_{0.1}T_z$ films with varying thicknesses in the X-, Ka-, and W-bands. b) Comparison of EMI SE elements in Cu and Al foils, and $Ti_3C_{1.9}N_{0.1}T_z$ film. c) Calculated reflectance (left) and transmittance (right) of the MXene film as functions of electrical conductivity and thickness at 10 GHz. d) Calculated EMI SE$_T$ of the MXene film as functions of electrical conductivity, frequency, and thickness. e, f) Benchmark plots of EMI SE$_T$ at the (e) X-band and (f) W-band for $Ti_3C_{1.9}N_{0.1}T_z$ films.

high-frequency applications (Figure 4f; Table S9, Supporting Information).

3. Conclusion

We have reported a breakthrough in MXene film conductivity of ≈35000 S cm^{-1} through N substitution at the X-site in XSS MAX phases. Synthesis of high-stoichiometric XSS MAX phases and the elucidation of the effects of N substitution on the properties of these phases resulted in the improvement of structural and electrical properties of the resulting XSS MXene films. The significance of these results lies not only in the advantageous physical properties of XSS MXenes but also in the exceptional performance of XSS MXenes in broadband EMI shielding even at reduced thicknesses as confirmed by our transfer-matrix simulations. With its demonstrated effectiveness across a wide range

of frequencies, MXenes are poised to expand their applicability from traditional lower-frequency domains such as the X-band to cutting-edge sub-THz technologies.

4. Experimental Section

Materials: Ti (−325 mesh, 99.5%), Al (−325 mesh, 99.5%), graphite (−325 mesh, 99.9995%), LiF (powder, 98.5%), HBr (solution, 48%), and HF (solution, 48%–51%) were purchased from Thermo Scientific. AlN (powder, 10 µm, 98%), LiCl (powder, 99%), and HCl (solution, 37%) were purchased from Sigma–Aldrich. LiBr (powder, 98%) was purchased from DJ Chemicals. Al (18 µm) foil was purchased from Lotte Aluminium. Cu (10 µm) foil was purchased from Nilaco. All materials were used directly without purification.

Synthesis of XSS MAX Phase: Ti, Al, AlN, and graphite powders were ball-milled in ethanol for 24 h at 250 rpm according to the specific molar ratios listed in Table S1 (Supporting Information). The resulting slurry was vacuum filtrated to remove ethanol and then dried in air for 12 h. The homogeneous powder mixture was cold-pressed into 15 mm cylindrical pellets under a pressure of 30 MPa. These pellets were placed in an alumina crucible, heated at a rate of 5 °C min^{-1} to the target temperature, and held for 2 h under an Ar flow. After sintering, the pellets were ground and sieved through a 400-mesh sieve. All samples underwent HCl treatment to eliminate intermetallic impurities.[13]

Synthesis of XSS $Ti_3C_{2-x}N_xT_z$: 1 g of $Ti_3AlC_{2-x}N_x$ was gradually added to an etchant containing 4 mL of HF, 13 mL of deionized (DI) water, and 13 mL of HCl, stirred continuously at 35 °C. The etching time was adjusted based on the value of x in $Ti_3AlC_{2-x}N_x$ (Figure S11, Supporting Information). The etched mixture was washed three times with DI water through centrifugation at 4500 rcf for 5 min using a 250 mL conical tube. The washed sediment was then redispersed in 40 mL of DI water containing 1 g of LiCl and stirred vigorously for 2 h using a vortex mixer. The mixture was centrifuged again at 4500 rcf for 5 min and washed three more times with DI water, resulting in spontaneous delamination. After self-delamination, the mixture was transferred to a 250 mL conical tube and centrifuged at 2500 rcf for 30 min to separate multi-layered MXene. The dark supernatant containing the delaminated 32-MXene was collected using a 250 mL flat tube and concentrated by centrifugation at 8000 rcf for 20 min. This process was repeated until the supernatant became sufficiently diluted. Finally, the concentrated MXene was washed three times with DI water to remove excess Li^+ ions, yielding 32-MXene for further use.

Synthesis of XSS $Ti_4C_{3-y}N_yT_z$: Synthesis of 43-MXene was performed using a saturated salt solution method. Specifically, 1 g of $Ti_4AlC_{3-y}N_y$ was slowly added to a solution containing 30 g of LiBr, 15 mL of DI water, 15 mL of HBr, and 2 g of LiF. The resulting mixture was transferred to a Teflon-lined autoclave, sealed, and heated to 80 °C for a duration dependent on the y content in $Ti_4AlC_{3-y}N_y$ (Figure S12, Supporting Information). The autoclave was then cooled to room temperature. The etched mixture was washed three times with DI water by centrifugation at 4500 rcf for 5 min, resulting in self-delamination. The delaminated 43-MXene was collected by centrifugation at 1500 rcf for 10 min to separate any unreacted MAX phase and LiF. The sample was then purified with DI water by centrifugation at 8000 rcf for 15 min to remove excess Li^+ ions from the solution, preparing the 43-MXene for further use.

Characterizations: The XRD patterns were recorded using a high-power XRD instrument (Rigaku, D/MAX2500V/PC) with Cu K_α radiation (40 kV, 200 mA) and a scan step of 0.02°. The morphologies of the samples were examined using SEM (SU7000, Hitachi) with an attached EDS detector. The thicknesses of the vacuum-filtrated MXene film were measured from cross-sectional SEM images using ImageJ software. Raman spectra of the MAX phase and MXene were obtained using an alpha300R (WITec) with a laser power of 5 mW and an alpha300S (WITec) with a laser power of 1 mW, both at an excitation wavelength of 532 nm. AFM images were acquired using a Bruker Dimension AFM instrument operating in tapping mode. The XPS data were collected using an ESCALAB 250XI instrument (ThermoFisher) equipped with a micro-focused monochromatic Al X-ray source under ultrahigh vacuum. The sheet resistance of MAX phases and MXene films was measured using a four-point probe (CMT2000N, AIT), with a highly p-doped Si substrate serving as the standard sample. The optical features were recorded using UV–vis NIR spectrometer (Cary 5000). EMI-shielding measurements were conducted using a two-port vector network analyzer (VNA, N5247A, Agilent), a millimeter head controller (N5261A, Agilent), a frequency extender (N5260-60003, Agilent), and rectangular waveguides for the X, K_a, and W bands, following standard calibration using Thru, Reflect, and Line (TRL) methods.

Computational Methods: All the DFT calculations were performed using the Vienna ab initio simulation package (VASP) code.[43] The calculations were performed within the generalized gradient approximation (GGA) of the Perdew–Burke–Ernzerhof (PBE) functional.[44] Reciprocal-space integration was performed using the Monkhorst-Pack scheme[45] with an accuracy of 0.06 $Å^{-1}$, and a plane-wave cutoff energy of 800 eV was used for lattice constant optimization and 400 eV for the other calculations. To determine the formation energy of the XSS MAX phases, nine 312- and 413-MAX phases with different C:N ratios and all possible 26 elemental/binary/ternary phases of the Ti-Al-C-N system were fully relaxed until the force on each atom was lower than 0.02 eV $Å^{-1}$. The SQS structures for the 312- and 413-MAX phases were generated using the MCSQS code,[46] and the supercell size was $5 \times 2 \times 1$.

Supporting Information

Supporting Information is available from the Wiley Online Library or from the author.

Acknowledgements

This work was supported by the Nano Material Technology Development Program (Grant No. RS-2024-00408180 (G.-D.L., E.C., S.-Y.K.)) through the National Research Foundation (NRF) of Korea funded by the Ministry of Science, ICT, and Future Planning.

Conflict of Interest

The authors declare no conflict of interest.

Author Contributions

J.-H.H., J.P., M.K., and S.L. are equally contibuted to this work. J.-H.H. and J.P. performed the experiments for this study with assistance from J.H., Y.H.J., Y.C., J.W., S.-H.S., Y.S.; M.K., J.M.H., G.B. and E.C. performed EMI-shielding measurements; S.L. and G.-D.L. conducted theoretical calculation and drafted the manuscript of the part; J.-H.H. conducted transfer-matrix simulations; J.-H.H. and S.-Y.K. wrote the manuscript; all authors revised and commented on the manuscript; S.-Y.K. planned and supervised the project.

Data Availability Statement

The data that support the findings of this study are available from the corresponding author upon reasonable request.

Keywords

conductivity, EMI shielding, MAX phase, MXene, nitrogen, X-site solid solution

Received: February 6, 2025
Revised: April 17, 2025
Published online:

[1] M. Tonouchi, *Nat. Photon.* **2007**, *1*, 97.
[2] B. Yao, W. Hong, T. Chen, Z. Han, X. Xu, R. Hu, J. Hao, C. Li, H. Li, S. E. Perini, M. T. Lanagan, S. Zhang, Q. Wang, H. Wang, *Adv. Mater.* **2020**, *32*, 1907499.
[3] A. Iqbal, T. Hassan, S. M. Naqvi, Y. Gogotsi, C. M. Koo, *Nat. Rev. Electr. Eng.* **2024**, *1*, 180.
[4] X.-Y. Wang, S.-Y. Laio, Y.-J. Wan, P.-L. Zhu, Y.-G. Hu, T. Zhao, R. Sun, C.-P. Wong, *J. Mater. Chem. C* **2022**, *10*, 44.
[5] R. Song, B. Mao, Z. Wang, Y. Hui, N. Zhang, R. Fang, J. Zhang, Y. Wu, Q. Ge, K. S. Novoselov, D. He, *Proc. Natl. Acad. Sci. U.S.A.* **2023**, *120*, 2209807120.
[6] F. Shahzad, M. Alhabeb, C. B. Hatter, B. Anasori, S. M. Hong, C. M. Koo, Y. Gogotsi, *Science* **2016**, *353*, 1137.
[7] A. Iqbal, F. Shahzad, K. Hantanasirisakul, M.-K. Kim, J. Kwon, J. Hong, H. Kim, D. Kim, Y. Gogotsi, C. M. Koo, *Science* **2020**, *369*, 446.
[8] M. Han, C. E. Shuck, R. Rakhmanov, D. Parchment, B. Anasori, C. M. Koo, G. Friedman, Y. Gogotsi, *ACS Nano* **2020**, *14*, 5008.
[9] M. Naguib, M. Kurtoglu, V. Presser, J. Lu, J. Niu, M. Heon, L. Hultman, Y. Gogotsi, M. W. Barsoum, *Adv. Mater.* **2011**, *23*, 4248.
[10] M. Downes, C. E. Shuck, B. McBride, J. Busa, Y. Gogotsi, *Nat. Protoc.* **2024**, *19*, 1807.
[11] Y. Zhang, K. Ruan, K. Zhou, J. Gu, *Adv. Mater.* **2023**, *35*, 2211642.
[12] A. Liu, H. Qiu, X. Lu, H. Guo, J. Hu, C. Liang, M. He, Z. Yu, Y. Zhang, J. Kong, J. Gu, *Adv. Mater.* **2025**, *37*, 2414085.
[13] T. S. Mathis, K. Maleski, A. Goad, A. Sarycheva, M. Anayee, A. C. Foucher, K. Hantanasirisakul, C. E. Shuck, E. A. Stach, Y. Gogotsi, *ACS Nano* **2021**, *15*, 6420.
[14] J.-H. Han, S.-H. Seok, Y. H. Jin, J. Park, Y. Lee, H. U. Yeo, J.-H. Back, Y. Sim, Y. Chae, J. Wang, G.-Y. Oh, W. Lee, S. H. Park, I.-C. Bang, J. H. Kim, S.-Y. Kwon, *Nat. Commun.* **2023**, *14*, 6957.
[15] T. Zhang, C. E. Shuck, K. Shevchuk, M. Anayee, Y. Gogotsi, *J. Am. Chem. Soc.* **2023**, *145*, 22374.
[16] K. R. G. Lim, M. Shekhirev, B. C. Wyatt, B. Anasori, Y. Gogotsi, Z. W. Seh, *Nat. Synth.* **2022**, *1*, 601.
[17] I. Shein, A. Ivanovskii, *Comput. Mater. Sci.* **2012**, *65*, 104.
[18] N. Zhang, Y. Hong, S. Yazdanparast, M. A. Zaeem, *2D Mater.* **2018**, *5*, 045004.
[19] W. Jindata, K. Hantanasirisakul, T. Eknapakul, J. D. Denlinger, S. Sangphet, S. Chaiyachad, C. Jaisuk, A. Rasritat, T. Sawasdee, H. Nakajima, *Appl. Phys. Rev.* **2021**, *8*, 021401.
[20] C. Yang, Y. Tang, Y. Tian, Y. Luo, M. Faraz Ud Din, X. Yin, W. Que, *Adv. Energy. Mater.* **2018**, *8*, 1802087.
[21] J. L. Hart, K. Hantanasirisakul, A. C. Lang, B. Anasori, D. Pinto, Y. Pivak, J. T. van Omme, S. J. May, Y. Gogotsi, M. L. Taheri, *Nat. Commun.* **2019**, *10*, 522.
[22] A. Iqbal, H. Kim, J. M. Oh, J. Chae, J. Kim, M. Kim, T. Hassan, Z. Gao, J. Lee, S. J. Kim, D. Kim, Y. Gogotsi, H. Kwon, C. M. Koo, *Small Methods* **2023**, *7*, 2201715.
[23] M. A. Pietzka, J. C. Schuster, *J. Am. Ceram. Soc.* **1996**, *79*, 2321.
[24] T. Cabioc'h, P. Eklund, V. Mauchamp, M. Jaouen, *J. Eur. Ceram. Soc.* **2012**, *32*, 1803.
[25] X. Qin, P. Zhang, S. Wang, Y. Du, Y. Zhang, Z. Sun, *Phys. Status Solidi B* **2017**, *254*, 1700009.
[26] B. Manoun, S. Saxena, G. Hug, A. Ganguly, E. Hoffman, M. Barsoum, *J. Appl. Phys.* **2007**, *101*, 113523.
[27] N. J. Lane, M. Naguib, V. Presser, G. Hug, L. Hultman, M. W. Barsoum, *J. Raman Spectrosc.* **2012**, *43*, 954.
[28] V. Presser, M. Naguib, L. Chaput, A. Togo, G. Hug, M. W. Barsoum, *J. Raman Spectrosc.* **2012**, *43*, 168.
[29] J.-U. Lee, S. Woo, J. Park, H. C. Park, Y.-W. Son, H. Cheong, *Nat. Commun.* **2017**, *8*, 1370.
[30] H. Ding, Y. Li, M. Li, K. Chen, K. Liang, G. Chen, J. Lu, J. Palisaitis, P. O. Persson, P. Eklund, *Science* **2023**, *379*, 1130.
[31] S.-H. Seok, Y. Sim, J.-H. Han, Y. H. Jin, Y. Chae, J. Park, S.-Y. Kwon, *Cell Rep. Phys. Sci.* **2023**, *4*, 101582.
[32] B. C. Wyatt, M. G. Boebinger, Z. D. Hood, S. Adhikari, P. P. Michałowski, S. K. Nemani, M. G. Muraleedharan, A. Bedford, W. J. Highland, P. R. Kent, *Nat. Commun.* **2024**, *15*, 6353.
[33] V. Natu, M. Benchakar, C. Canaff, A. Habrioux, S. Celerier, M. W. Barsoum, *Matter* **2021**, *4*, 1224.
[34] K. Matthews, T. Zhang, C. E. Shuck, A. VahidMohammadi, Y. Gogotsi, *Chem. Mater.* **2021**, *34*, 499.
[35] D. Magne, V. Mauchamp, S. Célérier, P. Chartier, T. Cabioc'h, *Phys. Rev. B: Condens. Matter* **2015**, *91*, 201409.
[36] G. Berdiyorov, *AIP Adv.* **2016**, *6*, 055105.
[37] D. Zhang, R. Wang, X. Wang, Y. Gogotsi, *Nat. Energy* **2023**, *8*, 567.
[38] A. A. Shamsabadi, H. Fang, D. Zhang, A. Thakur, C. Y. Chen, A. Zhang, H. Wang, B. Anasori, M. Soroush, Y. Gogotsi, *Small Methods* **2023**, *7*, 2300568.
[39] X. Sang, Y. Xie, M.-W. Lin, M. Alhabeb, K. L. Van Aken, Y. Gogotsi, P. R. Kent, K. Xiao, R. R. Unocic, *ACS Nano* **2016**, *10*, 9193.
[40] W. Zheng, B. Sun, D. Li, S. M. Gali, H. Zhang, S. Fu, L. Di Virgilio, Z. Li, S. Yang, S. Zhou, *Nat. Phys.* **2022**, *18*, 544.
[41] A. Thakur, N. B. S. Chandran, K. Davidson, A. Bedford, H. Fang, Y. Im, V. Kanduri, B. C. Wyatt, S. K. Nemani, V. Poliukhova, R. Kumar, Z. Fakhraai, B. Anasori, *Small Methods* **2023**, *7*, 2300030.
[42] S. Adomaviciute-Grabusove, A. Popov, S. Ramanavicius, V. Sablinskas, K. Shevchuk, O. Gogotsi, I. Baginskiy, Y. Gogotsi, A. Ramanavicius, *ACS Nano* **2024**, *18*, 13184.
[43] G. Kresse, J. Furthmüller, *Phys. Rev. B: Condens. Matter* **1996**, *54*, 11169.
[44] J. P. Perdew, K. Burke, M. Ernzerhof, *Phys. Rev. Lett.* **1996**, *77*, 3865.
[45] H. J. Monkhorst, J. D. Pack, *Phys. Rev. B: Condens. Matter* **1976**, *13*, 5188.
[46] A. Van de Walle, P. Tiwary, M. De Jong, D. Olmsted, M. Asta, A. Dick, D. Shin, Y. Wang, L.-Q. Chen, Z.-K. Liu, *Calphad* **2013**, *42*, 13.